

---

# FE-UNet: Frequency Domain Enhanced U-Net for Low-Frequency Information-Rich Image Segmentation

---

Guohao Huo<sup>1</sup>      Ruiting Dai<sup>1</sup>      Ling Shao<sup>2</sup>      Jinliang Liu<sup>1</sup>  
 Hao Tang<sup>3</sup> \*

<sup>1</sup> University of Electronic Science and Technology of China

<sup>2</sup> University of Chinese Academy of Sciences

<sup>3</sup> Peking University

gh.huo513@gmail.com, rtdai@uestc.edu.cn, ling.shao@ieee.org,  
 licaliu510@gmail.com, hao.tang@vision.ee.ethz.ch

## Abstract

In deep-sea exploration and surgical robotics scenarios, environmental lighting and device resolution limitations often cause high-frequency feature attenuation. Addressing the differences in frequency band sensitivity between CNNs and the human visual system (mid-frequency sensitivity with low-frequency sensitivity surpassing high-frequency), we experimentally quantified the CNN contrast sensitivity function and proposed a wavelet adaptive spectrum fusion (WASF) method inspired by biological vision mechanisms to balance cross-frequency image features. Furthermore, we designed a perception frequency block (PFB) that integrates WASF to enhance frequency-domain feature extraction. Based on this, we developed the FE-UNet model, which employs a SAM2 backbone network and incorporates fine-tuned Hiera-Large modules to ensure segmentation accuracy while improving generalization capability. Experiments demonstrate that FE-UNet achieves state-of-the-art performance in cross-domain tasks such as marine organism segmentation and polyp segmentation, showcasing robust adaptability and significant application potential.

## 1 Introduction

Image segmentation serves as a foundational task in computer vision, providing critical support for autonomous robotic Chen et al. [2025] systems such as surgical robots and deep-sea exploration robots to operate in complex environments. By isolating key features and structural details in images, this technology has demonstrated remarkable potential in cross-domain applications such as marine organism segmentation and polyp segmentation, significantly advancing the development of surgical robotics and deep-sea exploration systems. Although specialized architectures have achieved outstanding performance, critical challenges remain in overcoming low-frequency environments caused by seawater optical attenuation Chen et al. [2024] and high-frequency attenuation from surgical electrocoagulation particulates Kitrungrotsakul et al. [2019], both representing urgent technical bottlenecks.

Deep convolutional neural networks (CNNs) have markedly improved segmentation accuracy, yet their inherent bias toward high-frequency feature learning often leads to suboptimal performance in low-frequency dominant scenarios Tonkes and Sabatelli [2022], Bai et al. [2022]. For instance,

---

\*Corresponding author

in marine organism segmentation, underwater non-uniform illumination combined with seawater scattering/absorption/refraction induces high-frequency attenuation Chen et al. [2024]. Meanwhile, in polyp segmentation, uneven endoscopic lighting and scattering effects from electrocautery smoke amplify low-frequency components while suppressing high-frequency details Kitrungrotsakul et al. [2019], creating precision challenges for robotic surgical systems.

To address these issues, we propose FE-UNet - a novel feature learning framework specifically designed for low-frequency-dominant image segmentation. The framework enhances low-frequency information through Deep Wavelet Convolution (DWTConv) and employs spectral pooling filters to balance frequency components, mimicking the human visual system's mid-frequency sensitivity. The integrated Perception Frequency Block (PFB) with Wavelet-Adaptive Spectral Fusion (WASF) further enables multi-scale feature capture while simulating the receptive field-eccentricity relationship in biological vision. This synergy between CNN capabilities and visual system principles equips deep-sea exploration robots and surgical robots with human-like frequency-aware perception, significantly improving segmentation accuracy under challenging conditions.

In summary, our contributions are as follows: (1) We propose FE-UNet, a frequency domain-enhanced segmentation framework designed to improve segmentation performance by enhancing low-frequency feature information in low-quality images and balancing it with high-frequency features. (2) We introduce PFB (Perception Frequency Block), a module that aggregates frequency-domain feature balancing mechanisms, multi-scale receptive fields, and eccentricity-aware features inspired by the human visual system, enabling autonomous robots to acquire human-like visual feature capture capabilities. (3) We develop WASF (Wavelet-Adaptive Spectral Fusion), which strengthens low-frequency information and balances it with high-frequency features, providing a robust foundation for frequency-domain-aware feature learning. (4) Extensive experiments on four marine animal segmentation datasets and five polyp segmentation datasets demonstrate FE-UNet's state-of-the-art performance, validating its effectiveness in addressing precise segmentation challenges in environments with dominant low-frequency information or attenuated high-frequency details.

## 2 Related Work

### 2.1 Marine Animal Segmentation

Image segmentation technology is crucial for deep-sea exploration robots in marine animal recognition tasks Li et al. [2024], as it enables precise identification in complex underwater environments. In recent years, convolutional neural networks (CNNs) have been widely applied in marine animal segmentation. For instance, Li et al. [2022b] proposed an Enhanced Cascaded Decoder Network (ECDNet), while Li et al. [2021] introduced a feature interaction encoder with cascaded decoders to extract more comprehensive features for accurate segmentation in challenging underwater conditions. Similarly, Fu et al. [2024] designed a fusion network to learn the semantic features of marine animals.

Recently, the Segment Anything Model (SAM) has demonstrated remarkable segmentation capabilities. Based on this, Zhang et al. [2024] developed a dual-SAM architecture that integrates automatic prompting mechanisms to incorporate extensive prior information for underwater segmentation tasks. Furthermore, Yan et al. [2024] used the SAM encoder to generate multi-scale features and proposed a progressive prediction framework to enhance SAM's ability to capture global underwater information. Xiong et al. [2024] further utilized a U-Shape segmentation framework to augment SAM2's segmentation performance for high-quality marine animal delineation.

Despite these advancements, models relying on convolutional operations still face limitations due to marine refraction and scattering effects, which cause significant loss of high-frequency features in images. Since CNNs exhibit high sensitivity to high-frequency information, their capacity to capture semantic features remains constrained under such conditions. This challenge highlights the need for innovative approaches to address frequency-domain distortions caused by underwater light scattering and absorption phenomena.

### 2.2 Polyp Segmentation

Polyp segmentation in computer vision focuses on identifying and isolating polyp regions in medical images, which is crucial for surgical robots to recognize and differentiate polyp lesions from other tissues Jafar et al. [2024]. The main challenges arise from the diversity of polyp shapes, the ambiguity

of their boundaries, and the high similarity between polyps and surrounding tissues. Reference Zhou et al. [2023b] proposed a cross-level feature aggregation network that fuses multi-scale semantic information from different levels to achieve precise segmentation. However, this approach relies solely on convolutional neural networks (CNNs), limiting its ability to capture long-range dependencies within images. To address this limitation, He et al. [2023a] introduced an efficient integration of CNNs and Transformers for medical image segmentation. Yet during actual surgical robot operations, low-frequency environmental interference caused by uneven illumination and scattering effects of electrocautery smoke poses challenges to operational accuracy Wang et al. [2023a]. Traditional CNN- or Transformer-based models struggle to effectively capture low-frequency edge and detail information for polyp segmentation. To overcome this, we propose FE-UNet, which enhances low-frequency features through wavelet transformation for refined segmentation.

### 2.3 Frequency Domain Analysis

Frequency domain analysis has been extensively studied and applied in computer vision. Previous works Cooley et al. [1969], Deng and Cahill [1993] have shown that low-frequency features in natural images correspond to global structures and color information, while high-frequency features are associated with local edges, textures, and fine details. Studies such as Tonkes and Sabatelli [2022], Bai et al. [2022] have revealed that convolutional neural networks (CNNs) tend to exhibit a strong bias toward learning high-frequency features in visual data, but are less effective at capturing low-frequency representations. In contrast, multi-head self-attention mechanisms display the opposite tendency, favoring low-frequency features. WTConv Finder et al. [2024] introduced a method leveraging wavelet transforms to enhance low-frequency features in natural images, thus improving the capture of feature information over large receptive fields. To further utilize the frequency-domain characteristics of multi-head self-attention, LiTv2 Pan et al. [2022] proposed the HiLo attention mixer, which simultaneously captures both high-frequency and low-frequency information using self-attention. Meanwhile, SPAM Yun et al. [2023] developed a mixer that uses convolutional operations to balance high-frequency and low-frequency signals.

To the best of our knowledge, no prior work has specifically focused on enhancing low-frequency signals while effectively balancing high- and mid-frequency information. Inspired by this, we propose a novel mixer called Wavelet-Adaptive Spectral Fusion (WASF), which utilizes Deep Wavelet Convolution (DWT-Conv) to enhance low-frequency signals. Subsequently, spectral pooling filters are applied to the enhanced frequency-domain features to perform frequency mixing, enabling the effective capture and utilization of high-, mid- and low-frequency information in image representations. In addition, we are the first to propose a method that simulates the human visual system based on frequency information.

## 3 The Proposed Method

### 3.1 HVS-CNN Contrast Sensitivity Analysis

The human visual system's ability to discern details is closely related to the relative contrast of the observed area, typically represented by the Contrast Sensitivity Function (CSF) Matkovic et al. [2005]. The CSF is a function of spatial frequency and exhibits a band-pass characteristic. Based on extensive experiments, Mannos and Sakrison proposed a classic model for the Contrast Sensitivity Function:

$$H(f) = 2.6 * (0.192 + 0.114) * e^{[-(0.114f)^{1.1}]}, \quad (1)$$

where the spatial frequency is:

$$f = (f_x^2 + f_y^2)^{0.5}, \quad (2)$$

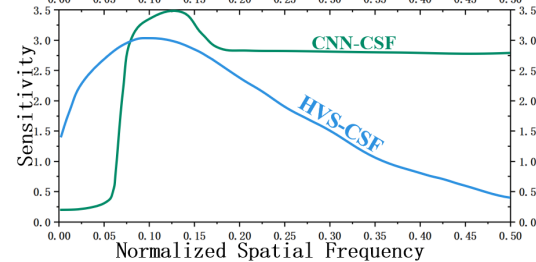


Figure 1: The Contrast Sensitivity Function model of the human visual system (HVS-CSF) and the Contrast Sensitivity Function model of convolutional neural networks (CNN-CSF), with the horizontal axis representing normalized spatial frequency and the vertical axis representing sensitivity.

where  $f_x$  and  $f_y$  represent the spatial frequencies in the horizontal and vertical directions, respectively, based on this, we plot the contrast sensitivity function (HVS-CSF) curve of the human visual system (see Figure 1). To compare the frequency characteristics of convolutional neural networks with those of the human visual system, we designed a simple classification experiment using the CIFAR-10 dataset Krizhevsky [2012]. We employ a pre-trained ResNet18 model on ImageNet for feature extraction and inference. For each channel of the image features, we sequentially applied the Fourier transform and circular masking.

$$F(u, v) = \int_{-\infty}^{\infty} \int_{-\infty}^{\infty} f(x, y) e^{-2\pi i(ux+vy)} dx dy, \quad (3)$$

$$M(u, v) = \begin{cases} 1 & \text{if } r \leq R; \\ 0 & \text{if } r > R. \end{cases}$$

Filter the image with different cutoff frequencies and then apply the inverse Fourier transform.

$$f_{\text{filtered}}(x, y) = \int_{-\infty}^{\infty} \int_{-\infty}^{\infty} F_{\text{filtered}}(u, v) e^{2\pi i(ux+vy)} du dv, \quad (4)$$

Convert the frequency-domain features back to the spatial domain and then measure the model’s classification accuracy at different cutoff frequencies. Plot the contrast sensitivity function (CNN-CSF) curve of the convolutional neural network in Figure 1. We can draw the following conclusions:

1. The human visual system is most sensitive to mid-frequency signals, with lower sensitivity to both low-frequency and high-frequency signals.
2. Similarly, convolutional neural networks exhibit low sensitivity to low-frequency signals. They are more responsive to mid-to-high-frequency signals, with a slightly greater sensitivity to mid-frequency signals compared to high-frequency signals.

Based on this, we propose the wavelet adaptive spectral fusion (WASF), which enhances low-frequency signals using a DWTConv. This is followed by mixing operations with a spectral pooling filter to blend high-frequency and low-frequency signals into the mid-frequency range, fully leveraging the convolutional module’s high sensitivity to mid-frequency signals.

To further simulate the human visual system, we propose the Perceptual Frequency Block (PFB). This module combines frequency domain information enhancement with the relationship between receptive field and eccentricity in the human visual system, achieving a more accurate simulation of the visual perception mechanism. Building on the PFB, the Hiera-L Block, and a U-shaped architecture, we have innovatively developed the FE-UNet architecture.

### 3.2 FE-UNet

The original SAM2 model generates segmentation results that are class-agnostic. Without manual prompts for specific classes, SAM2 cannot produce segmentation results for designated categories. To enhance the specificity of SAM2 and better adapt it to specific downstream tasks while efficiently using pre-trained parameters, we propose the FE-UNet architecture (as shown in Figure 2(a)). The architecture demonstrates robust segmentation capabilities for low-resolution images.

**Encoder.** FE-UNet leverages the pre-trained Hiera-L backbone network from SAM2. The attention mechanisms within the Hiera backbone address the limitations of traditional convolutional neural networks in capturing long-range contextual features. Furthermore, the hierarchical structure of the Hiera module facilitates the capture of multi-scale features, making it well-suited for designing U-shaped networks.

To achieve parameter-efficient fine-tuning, we design task-specific Res-Adapter and Mlp-Adapter with trainable parameters within the Hiera Block while keeping the parameters of the Hiera Block frozen. This approach eliminates the need to fine-tune the Hiera Block, significantly reducing memory consumption. Given an input image  $I \in R^{3 \times H \times W}$ , where  $H$  and  $W$  represent the height and width of the image, Hiera outputs four levels of hierarchical features  $X_i \in R^{C_i \times \frac{H}{2^{i+1}} \times \frac{W}{2^{i+1}}}$  ( $i \in \{1, 2, 3, 4\}$ ) The channel counts for each level are  $C_i \in \{144, 288, 576, 1152\}$

**Res-Adapter.** We drew inspiration from Houlsby et al. [2019], Qiu et al. [2023] to design the Res-Adapter module, which consists of a sequential structure: a linear layer for downsampling, a

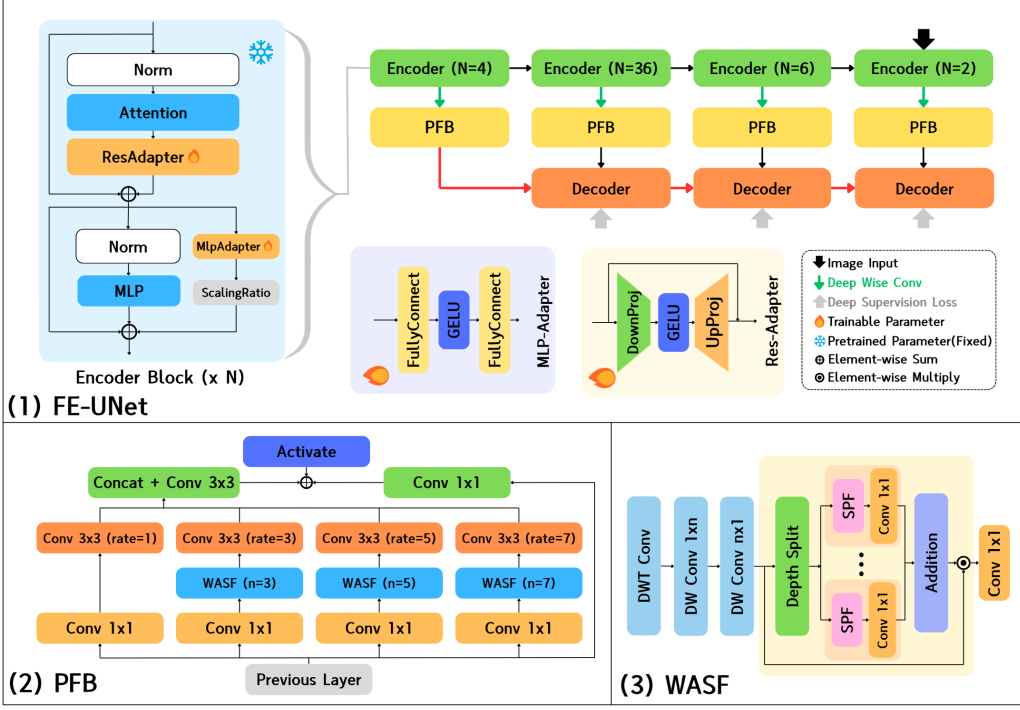


Figure 2: Fig. (a), (b), and (c) depict the architectures of the proposed FE-UNet model, Perception Frequency Block (PFB), and Wavelet-Adaptive Spectral Fusion (WASF), respectively.

GeLU activation function, and a linear layer for upsampling. To enable the Adapter to sufficiently fine-tune the output features of the attention mechanism, we initialize the parameters of Res-Adapter to zero. Additionally, residual connections are incorporated to mitigate the potential exponential gradient decay in single-chain paths that may arise from zero initialization. This design enables efficient fine-tuning of the Hiera Block while minimizing memory usage.

**Mlp-Adapter.** Inspired by the works of Wu et al. [2023b], Rebuffi et al. [2018], we design the Mlp-Adapter, which operates in parallel with both the pretrained MLP and residual connections. This design aims to address two key limitations in existing architectures: the pretrained MLP’s insufficient capacity to capture semantic feature relationships in task-specific segmentation scenarios, and the constrained non-linear modeling ability of parallel residual connections when handling complex feature interactions. Mlp-Adapter preserves backbone network information flow through parallel computation paths while enabling efficient adaptation via lightweight MLP operations, achieving enhanced feature refinement with minimal memory overhead.

**PFB.** After completing feature extraction at the encoder stage, the hierarchical features of the U-shaped network undergo multi-channel fusion through depthwise convolution, which compresses the channel count to 64. This channel fusion operation effectively reduces the GPU memory consumption of the subsequent Perceptual Frequency Block (PFB). The fused hierarchical features are then fed into the PFB, which simulates characteristics of the human visual system while emphasizing feature enhancement in the frequency domain.

**Decoder.** We made adjustments to the decoder part of the traditional UNet architecture, using the same upsampling operations. However, we implemented a customized DoubleConv module, which consists of two identical convolution—batch normalization—ReLU activation function combinations. The convolution operations use a kernel size of 3x3. Each decoder output feature is processed through a 1x1 convolutional segmentation head to generate segmentation results  $S_i (i \in \{1, 2, 3\})$ . These segmentation results are then upsampled and supervised against the ground truth segmentation masks.

**Loss Function.** Each hierarchical structure loss function in FE-UNet is composed of a weighted Intersection over Union (IoU) and Binary Cross-Entropy (BCE) loss. The specific single-level loss

function is defined as follows:

$$L = L_{IoU}^w + L_{BCE}^w. \quad (5)$$

Since we employ deep supervision, the final loss function for FE-UNet is expressed as the sum of the individual hierarchical losses:

$$L_{total} = \sum_{i=1}^3 L(G, S_i). \quad (6)$$

### 3.3 PFB

The human visual system’s ability to capture semantic information in natural images varies across different frequency domains. Generally, the human visual system (HVS) is most sensitive to mid-frequency signals, with higher sensitivity to low-frequency signals compared to high-frequency ones. In contrast, convolution operations typically exhibit greater sensitivity to mid-to-high-frequency signals than to low-frequency signals.

To fully utilize the characteristics of convolutional operations and the sensitivity of the human visual system to mid-frequency information, we employ Wavelet-Adaptive Spectral Fusion (WASF) to enhance low-frequency components in image features while performing adaptive fusion operations with high-frequency information. This process shifts the frequency characteristics of image features toward the mid-frequency range, thereby achieving simulation effects that simulate the receptive fields and eccentricity mechanisms of the human visual system. It also enhances the ability of subsequent convolutional operations to extract feature information.

To achieve multi-scale receptive field capture, we employ the wavelet-adaptive spectral fusion (WASF) with different depths and convolution kernel sizes. In the WASF,  $n$  represents the radius size of the low-frequency region  $\mathbf{A}^{lf}$  centered at the origin, which is  $2^n$ . The depth convolution part of the WASF is configured with kernel sizes of  $1 \times n$  and  $n \times 1$ . Subsequently, the padding numbers and dilation rates for the different branches of the dilated convolutions are set to  $rate = 1, 3, 5, 7$ . This configuration facilitates expansion of the receptive field and aligns the feature sizes, making it convenient for subsequent concatenation operations. As a result, we propose the PFB, with the structural diagram illustrated in Figure 2(b).

### 3.4 WASF

In the field of computer vision, two common image filtering methods are used: one involves kernel convolution in the spatial domain, while the other utilizes the Fourier transform for filtering in the frequency domain. The method proposed in this paper also operates in the frequency domain, but to achieve simple and efficient deep aggregation of spectral information under different receptive fields, we employ wavelet filtering. By applying a multi-branch spectral pooling filter followed by mixing operations on the Deep Wavelet Convolution (DWTConv), we introduce the Wavelet-Adaptive Spectral Fusion (WASF). The module architecture is shown in Figure 2(c).

**DWTConv.** To fully utilize low-frequency features, we employ specific cascaded deep-wavelet convolution operations. Similarly to WTConv Finder et al. [2024], we only made minor modifications to its implementation, with detailed descriptions provided in the supplementary material.

**SPF.** Based on the inverse power law, the most important visual information in natural images is concentrated in the mid-frequency region. After using the DWTConv, we employ spectral pooling filters to perform mixing operations on the low-frequency and high-frequency components in the spectrum, thereby increasing the weight of the low-frequency components. First, we use a two-dimensional DFT to map the features obtained after deep convolution from the spatial domain to the frequency domain:

$$Z = \mathcal{F}(z) \in \mathbb{C}^{H \times W}. \quad (7)$$

In the above formula,  $\mathcal{F}(\cdot)$  represents the two-dimensional DFT operation. Next, we perform a shifting operation to move the low-frequency components to the center of the spectrum. We then use a Fourier transform centering function to remove the remaining parts outside of the low-frequency subset.

$$S^{lf} = \begin{cases} \mathcal{G}(Z)(u, v), & \text{if } (u, v) \in \mathbf{A}^{lf} \\ 0, & \text{else} \end{cases} \quad (8)$$

In the above formula,  $\mathcal{G}(\cdot)$  is the Fourier transform centering function,  $(u, v)$  is a pair of positions in the frequency domain, and  $\mathbf{A}^{lf} \in \mathbb{R}^2$  represents the low-frequency region centered at the origin.

High-pass filters are the opposite of low-pass filters, so high-frequency components can be directly obtained by removing low-frequency components from the input feature map:

$$S^{hf} = \mathcal{G}(Z) - S^{lf}. \quad (9)$$

Finally, by sequentially applying the inverse transformation and inverse DFT operation to the high-frequency and low-frequency components, we can obtain the spectral pooled feature map:

$$f_{lp}(Z) = \mathcal{F}^{-1}(\mathcal{G}^{-1}(S^{lf})) \in \mathbb{R}^{H \times W}, \quad (10)$$

$$f_{hp}(Z) = \mathcal{F}^{-1}(\mathcal{G}^{-1}(S^{hf})) \in \mathbb{R}^{H \times W}. \quad (11)$$

We mix the visual features of different frequency bands obtained from the decomposition using a combination filter, which can be represented by the following formula:

$$\tilde{Z} = \lambda f_{lp}(Z) + (1 - \lambda) f_{hp}(Z) \in \mathbb{R}^{H \times W}. \quad (12)$$

Since  $\mathcal{F}(\cdot)$  and  $\mathcal{G}(\cdot)$ , as well as their inverses, are linear operations, they satisfy the principle of superposition. The above formula is equivalent to:

$$\tilde{Z} = \mathcal{F}^{-1}(\mathcal{G}^{-1}(\lambda S^{lf} + (1 - \lambda) S^{hf})), \quad (13)$$

where  $\lambda \in [0, 1]$  is a balancing parameter. We can now manipulate the frequency spectrum of visual features by adjusting  $\lambda$  to control the balance between the high-frequency and low-frequency components.

## 4 Experiments

Following the convention of SPANet Yang et al. [2022], Yun et al. [2023], we experimentally validated the effectiveness of FE-UNet on two tasks: marine animal segmentation and polyp segmentation. For the marine animal segmentation task, we employed five evaluation metrics—mean Intersection over Union (mIoU), S-measure ( $S_\alpha$ ), weighted F-measure ( $F_\beta^w$ ), mean E-measure ( $mE_\phi$ ), and mean absolute error (MAE)—to assess model performance. In the polyp segmentation task, model effectiveness was evaluated using two key metrics: mean Dice score (mDice) and mIoU. Detailed implementation details and dataset configurations are provided in the Supplementary Material.

**Comparison with State-of-the-Arts.** In this section, we compare our method with other approaches on four public marine animal segmentation datasets and five public polyp segmentation datasets. The quantitative and qualitative results clearly demonstrate the significant advantages of our proposed method.

**Quantitative Comparison** Tables 1 and 2 present quantitative comparisons of typical marine animal segmentation datasets. Compared with CNN-based methods, our method significantly improves performance. On the challenging MAS3K dataset, our method achieves the highest scores across all metrics, delivering a 4-6% improvement. Moreover, our method consistently outperforms others on additional MAS datasets. Compared to state-of-the-art marine animal segmentation models, our model achieves a 1-2% improvement in mIoU and  $S_\alpha$  metrics. Compared with Transformer-based methods, our method achieves a 3-6% improvement on the MAS3K dataset. Furthermore, compared with other SAM-based methods, our model achieves a 1-2% improvement in mIoU scores as well as  $S_\alpha$  compared to current SOTA methods.

We follow Zhou et al. [2023a], including the same comparison methods and tools. Table 3 shows the performance of our model on five polyp segmentation test datasets. On the Kvasir, CVC-ClinicDB, and CVC-300 datasets, our model achieved SOTA performance, with a 1-2% improvement over the second-best method. Furthermore, on the CVC-ColonDB and ETIS datasets, our model demonstrated the second-best segmentation performance.

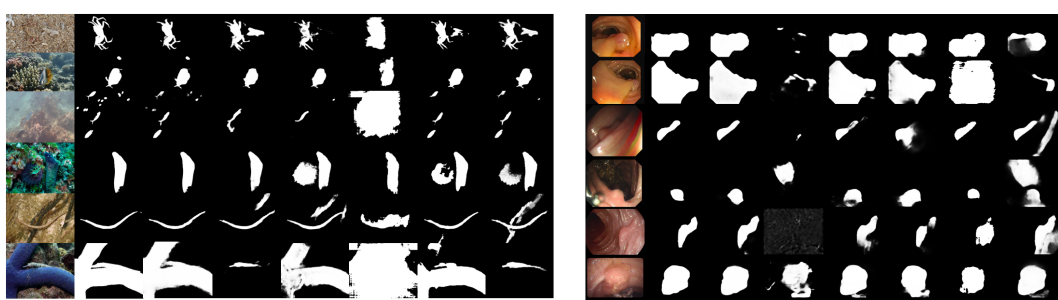
**Qualitative Comparison** Figures 3 illustrate some visual examples from the marine animal segmentation and polyp segmentation tasks, respectively, to further verify the effectiveness of our method. Compared with previous approaches, our method produces segmentation results that are highly similar to the ground truth in simpler tasks. Moreover, on challenging images with cluttered backgrounds and rich details, our method consistently generates more accurate and refined segmentation masks.

Table 1: Marine animal segmentation performance on MAS3K and RMAS datasets.

Category	Method	MAS3K					RMAS				
		mIoU	$S_\alpha$	$F_\beta^w$	$mE_\phi$	MAE	mIoU	$S_\alpha$	$F_\beta^w$	$mE_\phi$	MAE
CNN	PFANet Zhao and Wu [2019]	0.405	0.690	0.471	0.768	0.086	0.556	0.767	0.582	0.810	0.051
	SCRN Wu et al. [2019]	0.693	0.839	0.730	0.869	0.041	0.695	0.842	0.731	0.878	0.030
	UNet++ Zhou et al. [2020]	0.506	0.726	0.552	0.790	0.083	0.558	0.763	0.644	0.835	0.046
	U2Net Qin et al. [2020]	0.654	0.812	0.711	0.851	0.047	0.676	0.830	0.762	0.904	0.029
	SINet Fan et al. [2020b]	0.658	0.820	0.725	0.884	0.039	0.684	0.835	0.780	0.908	0.025
	BASNet Piao et al. [2021]	0.677	0.826	0.724	0.862	0.046	0.707	0.847	0.771	0.907	0.032
	PFNet Mei et al. [2021]	0.695	0.839	0.746	0.890	0.039	0.694	0.843	0.771	0.922	0.026
	RankNet Lv et al. [2021b]	0.658	0.812	0.722	0.867	0.043	0.704	0.846	0.772	0.927	0.026
	C2FNet Sun et al. [2021]	0.717	0.851	0.761	0.894	0.038	0.721	0.858	0.788	0.923	0.026
	ECDFNet Li et al. [2022b]	0.711	0.850	0.766	0.901	0.036	0.664	0.823	0.689	0.854	0.036
	OCENet Liu et al. [2022]	0.667	0.824	0.703	0.868	0.052	0.680	0.836	0.752	0.900	0.030
Transformer	ZoomNet Pang et al. [2022]	0.736	0.862	0.780	0.898	0.032	0.728	0.855	0.795	0.915	0.022
	MASNet Fu et al. [2024]	0.742	0.864	0.788	0.906	0.032	0.731	0.862	0.801	0.920	0.024
SAM	SETR Zheng et al. [2021]	0.715	0.855	0.789	0.917	0.030	0.654	0.818	0.747	0.933	0.028
	TransUNet Chen et al. [2021]	0.739	0.861	0.805	0.919	0.029	0.688	0.832	0.776	0.941	0.025
	H2Former He et al. [2023a]	0.748	0.865	0.810	0.925	0.028	0.717	0.844	0.799	0.931	0.023
	SAM Kirillov et al. [2023]	0.566	0.763	0.656	0.807	0.059	0.445	0.697	0.534	0.790	0.053
	Med-SAM Wu et al. [2023a]	0.739	0.861	0.811	0.922	0.031	0.678	0.832	0.778	0.920	0.027
	SAM-Adapter Chen et al. [2023]	0.714	0.847	0.782	0.914	0.033	0.656	0.816	0.752	0.927	0.027
	SAM-DADF La et al. [2023]	0.742	0.866	0.806	0.925	0.028	0.686	0.833	0.780	0.926	0.024
	I-MedSAM Wei et al. [2024]	0.698	0.835	0.759	0.889	0.039	0.633	0.803	0.699	0.893	0.035
	Dual-SAM Zhang et al. [2024]	0.799	0.884	0.838	0.933	0.023	0.735	0.860	0.812	0.944	0.022
	MAS-SAM Yan et al. [2024]	0.788	0.887	0.840	0.938	0.025	0.742	0.865	0.819	0.948	0.021
	SAM2-UNet Xiong et al. [2024]	0.799	<b>0.903</b>	<b>0.848</b>	<b>0.943</b>	<b>0.021</b>	0.738	<b>0.874</b>	0.810	0.944	0.022
	FE-UNet (Ours)	<b>0.815</b>	0.900	<b>0.848</b>	0.928	0.022	<b>0.758</b>	<b>0.874</b>	0.811	0.938	<b>0.021</b>

Table 2: Marine animal segmentation performance on UFO120 and RUWI datasets.

Category	Method	UFO120					RUWI				
		mIoU	$S_\alpha$	$F_\beta^w$	$mE_\phi$	MAE	mIoU	$S_\alpha$	$F_\beta^w$	$mE_\phi$	MAE
CNN	PFANet Zhao and Wu [2019]	0.677	0.752	0.723	0.815	0.129	0.773	0.765	0.811	0.867	0.096
	SCRN Wu et al. [2019]	0.678	0.783	0.760	0.839	0.106	0.830	0.847	0.883	0.925	0.059
	UNet++ Zhou et al. [2020]	0.412	0.459	0.433	0.451	0.409	0.586	0.714	0.678	0.790	0.145
	U2Net Qin et al. [2020]	0.680	0.792	0.709	0.811	0.134	0.841	0.873	0.861	0.786	0.074
	SINet Fan et al. [2020b]	0.767	0.837	0.834	0.890	0.079	0.785	0.789	0.825	0.872	0.096
	BASNet Piao et al. [2021]	0.710	0.809	0.793	0.865	0.097	0.841	0.871	0.895	0.922	0.056
	PFNet Mei et al. [2021]	0.570	0.708	0.550	0.683	0.216	0.864	0.883	0.870	0.790	0.062
	RankNet Lv et al. [2021b]	0.739	0.823	0.772	0.828	0.101	0.865	0.886	0.889	0.759	0.056
	C2FNet Sun et al. [2021]	0.747	0.826	0.806	0.878	0.083	0.840	0.830	0.883	0.924	0.060
	ECDFNet Li et al. [2022b]	0.693	0.783	0.768	0.848	0.103	0.829	0.812	0.871	0.917	0.064
	OCENet Liu et al. [2022]	0.605	0.725	0.668	0.773	0.161	0.763	0.791	0.798	0.863	0.115
Transformer	ZoomNet Pang et al. [2022]	0.616	0.702	0.670	0.815	0.174	0.739	0.753	0.771	0.817	0.137
	MASNet Fu et al. [2024]	0.754	0.827	0.820	0.879	0.083	0.865	0.880	0.913	0.944	0.047
	SETR Zheng et al. [2021]	0.711	0.811	0.796	0.871	0.089	0.832	0.864	0.895	0.924	0.055
	TransUNet Chen et al. [2021]	0.752	0.825	0.827	0.888	0.079	0.854	0.872	0.910	0.940	0.048
	H2Former He et al. [2023a]	0.780	0.844	0.845	<b>0.901</b>	0.070	0.871	0.884	0.919	0.945	0.045
	SAM Kirillov et al. [2023]	0.681	0.768	0.745	0.827	0.121	0.849	0.855	0.907	0.929	0.057
	Med-SAM Wu et al. [2023a]	0.774	0.842	0.839	0.899	0.072	0.877	0.885	0.921	0.942	0.045
	SAM-Adapter Chen et al. [2023]	0.757	0.829	0.834	0.884	0.081	0.867	0.878	0.913	0.946	0.046
	SAM-DADF La et al. [2023]	0.768	0.841	0.836	0.893	0.073	0.881	0.889	0.925	0.940	0.044
	I-MedSAM Wei et al. [2024]	0.730	0.818	0.788	0.865	0.084	0.844	0.849	0.897	0.923	0.050
	Dual-SAM Zhang et al. [2024]	0.810	0.856	<b>0.864</b>	<b>0.914</b>	0.064	0.904	0.903	0.939	0.959	<b>0.035</b>
	MAS-SAM Yan et al. [2024]	0.807	0.861	<b>0.864</b>	<b>0.914</b>	<b>0.063</b>	0.902	0.894	<b>0.941</b>	<b>0.961</b>	<b>0.035</b>
	SAM2-UNet Xiong et al. [2024]	0.810	0.858	0.845	0.889	0.072	0.906	0.903	0.927	0.941	0.037
	FE-UNet (Ours)	<b>0.821</b>	<b>0.871</b>	<b>0.856</b>	<b>0.914</b>	0.067	<b>0.914</b>	<b>0.912</b>	0.936	0.959	0.037



(a) Marine animal segmentation task

(b) Polyp segmentation task

Figure 3: Qualitative Comparative

Table 3: Polyp segmentation performance on Kvasir-SEGJha et al. [2020], CVC-ClinicDBBernal et al. [2015], CVC-ColonDBTajbakhsh et al. [2016], CVC-300Vázquez et al. [2016], and ETISSilva et al. [2014] datasets.

Method	Kvasir		CVC-ClinicDB		CVC-ColonDB		CVC-300		ETIS	
	mDice	mIoU								
UNetRonneberger et al. [2015]	0.818	0.746	0.823	0.755	0.504	0.436	0.710	0.627	0.398	0.335
SFAFang et al. [2019]	0.723	0.611	0.700	0.607	0.456	0.337	0.467	0.329	0.297	0.217
UNet++Zhou et al. [2020]	0.821	0.744	0.794	0.729	0.482	0.408	0.707	0.624	0.401	0.344
PraNetFan et al. [2020c]	0.898	0.840	0.899	0.849	0.709	0.640	0.871	0.797	0.628	0.567
EU-NetPatel et al. [2021]	0.908	0.854	0.902	0.846	0.756	0.681	0.837	0.765	0.687	0.609
SANetWei et al. [2021]	0.904	0.847	0.916	0.859	0.752	0.669	0.888	0.815	0.750	0.654
MSNetZhao et al. [2021]	0.905	0.849	0.918	0.869	0.751	0.671	0.865	0.799	0.723	0.652
C2FNetSun et al. [2021]	0.886	0.831	0.919	0.872	0.724	0.650	0.874	0.801	0.699	0.624
MSEGLiao et al. [2022]	0.897	0.839	0.909	0.864	0.735	0.666	0.874	0.804	0.700	0.630
DCRNetYin et al. [2022]	0.886	0.825	0.896	0.844	0.704	0.631	0.856	0.788	0.556	0.496
LDNetZhang et al. [2022]	0.887	0.821	0.881	0.825	0.740	0.652	0.869	0.793	0.645	0.551
FAPNetZhou et al. [2022]	0.902	0.849	0.925	0.877	0.731	0.658	0.893	0.826	0.717	0.643
ACSNetZhang et al. [2023]	0.898	0.838	0.882	0.826	0.716	0.649	0.863	0.787	0.578	0.509
H2Former He et al. [2023a]	0.910	0.858	0.922	0.871	0.719	0.642	0.856	0.793	0.614	0.547
CaraNetLou et al. [2023]	0.913	0.859	0.921	0.876	0.775	0.700	0.902	0.836	0.740	0.660
CFA-NetZhou et al. [2023b]	0.915	0.861	0.933	0.883	0.743	0.665	0.893	0.827	0.732	0.655
I-MedSAMWei et al. [2024]	0.839	0.759	0.871	0.788	<b>0.885</b>	<b>0.800</b>	0.900	0.822	<b>0.874</b>	<b>0.791</b>
SAM2-UNetXiong et al. [2024]	0.928	0.879	0.907	0.856	0.808	0.730	0.894	0.827	0.796	0.723
FE-UNet(Ours)	<b>0.934</b>	<b>0.889</b>	<b>0.942</b>	<b>0.895</b>	0.830	0.757	<b>0.914</b>	<b>0.852</b>	0.819	0.748

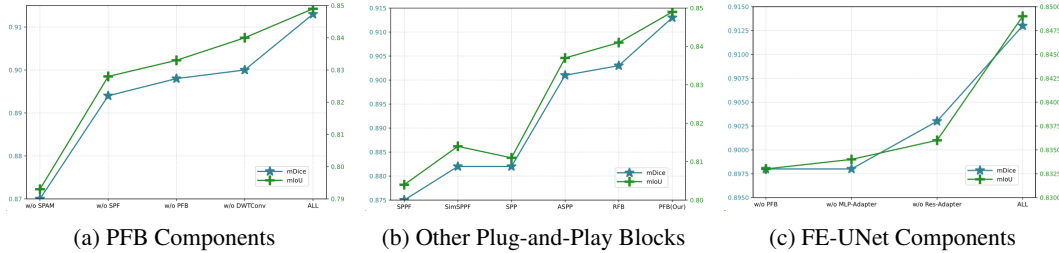


Figure 4: Visualization of Ablation Experiment Results

#### 4.1 Ablation Study

As shown in the figure 4, we conducted three groups of ablation experiments on the CVC-300 dataset to validate the effectiveness of key components in FE-UNet. First, we assessed the necessity of each component in the PFB module, demonstrating that all elements are essential for optimal performance. Second, we compared PFB against mainstream multi-scale feature extraction modules (SPPF Khanam and Hussain [2024], SimSPPF Li et al. [2022a], SPP He et al. [2015], ASPP Chen et al. [2018], and RFB Liu et al. [2018]) when integrated into FE-UNet’s residual connections, with PFB achieving superior multi-scale feature extraction capability. Finally, we verified the necessity of all FE-UNet components by individually removing PFB, MLP-Adapter, and Res-Adapter, observing significant performance degradation in each case, thereby confirming the indispensability of every element in the architecture.

### 5 Conclusion

In this work, we propose a novel feature learning framework named FE-UNet for natural image segmentation. Specifically, we introduce the Perceptual Frequency Block (PFB), which aggregates frequency-domain information enhanced by multi-scale WASF modules through the integration of multi-scale receptive fields and eccentricity-aware mechanisms. This design simulates the human visual system’s heightened sensitivity to mid-frequency features, enabling our method to extract rich frequency-domain features critical for fine-grained image segmentation. Experimental results demonstrate state-of-the-art (SOTA) performance in the marine animal segmentation and polyp segmentation task. Our framework is not only applicable to marine animal and medical polyp segmentation scenarios but also lays a solid foundation for image segmentation in other complex scenarios, providing a broader research space for enhancing visual perception capabilities in autonomous robots such as surgical and deep-sea exploration systems.

## References

Jiawang Bai, Li Yuan, Shu-Tao Xia, Shuicheng Yan, Zhifeng Li, and Wei Liu. Improving vision transformers by revisiting high-frequency components. In *ECCV 2022*, volume 13684, pages 1–18. Springer, 2022.

Jorge Bernal, Francisco Javier Sánchez, Gloria Fernández-Esparrach, Debora Gil, Cristina Rodríguez de Miguel, and Fernando Vilariño. WM-DOVA maps for accurate polyp highlighting in colonoscopy: Validation vs. saliency maps from physicians. *Comput. Medical Imaging Graph.*, 43: 99–111, 2015.

Jieneng Chen, Yongyi Lu, Qihang Yu, Xiangde Luo, Ehsan Adeli, Yan Wang, Le Lu, Alan L. Yuille, and Yuyin Zhou. Transunet: Transformers make strong encoders for medical image segmentation. *CoRR*, abs/2102.04306, 2021.

Liang-Chieh Chen, George Papandreou, Iasonas Kokkinos, Kevin Murphy, and Alan L. Yuille. Deeplab: Semantic image segmentation with deep convolutional nets, atrous convolution, and fully connected crfs. *IEEE Trans. Pattern Anal. Mach. Intell.*, 40(4):834–848, 2018.

Siyu Chen, Lin Deng, and Jun Zhao. Enhanced reconstruction of satellite-derived monthly chlorophyll a concentration with fourier transform convolutional-lstm. *IEEE Trans. Geosci. Remote. Sens.*, 62: 1–14, 2024.

Tianrun Chen, Lanyun Zhu, Chaotao Ding, Runlong Cao, Yan Wang, Zejian Li, Lingyun Sun, Papa Mao, and Ying Zang. SAM fails to segment anything? - sam-adapter: Adapting SAM in underperformed scenes: Camouflage, shadow, and more. *CoRR*, abs/2304.09148, 2023.

Yinglong Chen, Fei Gao, Cheng Zhou, Xinyu Yang, Xingtian Xiao, and Bo Yan. Technology and equipment for underwater robots. *Journal of Marine Science and Engineering*, 13(4), 2025.

James W. Cooley, Peter A. W. Lewis, and Peter D. Welch. The fast fourier transform and its applications. *IEEE Transactions on Education*, 12(1):27–34, 1969.

Cheng Deng, Xu Yang, Feiping Nie, and Dapeng Tao. Saliency detection via a multiple self-weighted graph-based manifold ranking. *IEEE Trans. Multim.*, 22(4):885–896, 2020.

G. Deng and L.W. Cahill. An adaptive gaussian filter for noise reduction and edge detection. In *1993 IEEE Conference Record Nuclear Science Symposium and Medical Imaging Conference*, pages 1615–1619 vol.3, 1993.

Deng-Ping Fan, Ge-Peng Ji, Guolei Sun, Ming-Ming Cheng, Jianbing Shen, and Ling Shao. Camouflaged object detection. In *2020 IEEE/CVF Conference on Computer Vision and Pattern Recognition, CVPR 2020, Seattle, WA, USA, June 13-19, 2020*, pages 2774–2784. Computer Vision Foundation / IEEE, 2020a.

Deng-Ping Fan, Ge-Peng Ji, Guolei Sun, Ming-Ming Cheng, Jianbing Shen, and Ling Shao. Camouflaged object detection. In *CVPR 2020*, pages 2774–2784. Computer Vision Foundation / IEEE, 2020b.

Deng-Ping Fan, Ge-Peng Ji, Tao Zhou, Geng Chen, Huazhu Fu, Jianbing Shen, and Ling Shao. Planet: Parallel reverse attention network for polyp segmentation. In *MICCAI 2020*, volume 12266, pages 263–273. Springer, 2020c.

Yuqi Fang, Cheng Chen, Yixuan Yuan, and Raymond Kai-Yu Tong. Selective feature aggregation network with area-boundary constraints for polyp segmentation. In *MICCAI 2019*, volume 11764, pages 302–310. Springer, 2019.

Shahaf E. Finder, Roy Amoyal, Eran Treister, and Oren Freifeld. Wavelet convolutions for large receptive fields. In *ECCV 2024*, volume 15112, pages 363–380. Springer, 2024.

Zhenqi Fu, Ruizhe Chen, Yue Huang, En Cheng, Xinghao Ding, and Kai-Kuang Ma. Masnet: A robust deep marine animal segmentation network. *IEEE Journal of Oceanic Engineering*, 49(3): 1104–1115, 2024.

Along He, Kai Wang, Tao Li, Chengkun Du, Shuang Xia, and Huazhu Fu. H2former: An efficient hierarchical hybrid transformer for medical image segmentation. *IEEE Trans. Medical Imaging*, 42(9):2763–2775, 2023a.

Chunming He, Kai Li, Yachao Zhang, Longxiang Tang, Yulun Zhang, Zhenhua Guo, and Xiu Li. Camouflaged object detection with feature decomposition and edge reconstruction. In *Proceedings of the IEEE/CVF conference on computer vision and pattern recognition*, pages 22046–22055, 2023b.

Kaiming He, Xiangyu Zhang, Shaoqing Ren, and Jian Sun. Spatial pyramid pooling in deep convolutional networks for visual recognition. *IEEE Trans. Pattern Anal. Mach. Intell.*, 37(9):1904–1916, 2015.

Neil Houlsby, Andrei Giurgiu, Stanislaw Jastrzebski, Bruna Morrone, Quentin de Laroussilhe, Andrea Gesmundo, Mona Attariyan, and Sylvain Gelly. Parameter-efficient transfer learning for NLP. In *ICML 2019*, volume 97, pages 2790–2799. PMLR, 2019.

Abbas Jafar, Zain Ul Abidin, Rizwan Ali Naqvi, and Seung-Won Lee. Unmasking colorectal cancer: A high-performance semantic network for polyp and surgical instrument segmentation. *Eng. Appl. Artif. Intell.*, 138, 2024.

Debesh Jha, Pia H. Smedsrød, Michael A. Riegler, Pål Halvorsen, Thomas de Lange, Dag Johansen, and Håvard D. Johansen. Kvasir-seg: A segmented polyp dataset. In *MMM 2020*, pages 451–462. Springer, 2020.

Rahima Khanam and Muhammad Hussain. What is yolov5: A deep look into the internal features of the popular object detector. *arXiv preprint arXiv:2407.20892*, 2024.

Alexander Kirillov, Eric Mintun, Nikhila Ravi, Hanzi Mao, Chloé Rolland, Laura Gustafson, Tete Xiao, Spencer Whitehead, Alexander C. Berg, Wan-Yen Lo, Piotr Dollár, and Ross B. Girshick. Segment anything. In *ICCV 2023*, pages 3992–4003. IEEE, 2023.

Titinunt Kitrungrotsakul, Xian-Hua Han, Yutaro Iwamoto, Lanfen Lin, Amir Hossein Foruzan, Wei Xiong, and Yen-Wei Chen. Vesselnet: A deep convolutional neural network with multi pathways for robust hepatic vessel segmentation. *Comput. Medical Imaging Graph.*, 75:74–83, 2019.

Alex Krizhevsky. Learning multiple layers of features from tiny images. *University of Toronto*, 05 2012.

Yingxin Lai, Zhiming Luo, and Zitong Yu. Detect any deepfakes: Segment anything meets face forgery detection and localization. In *CCBR 2023*, volume 14463, pages 180–190. Springer, 2023.

Trung-Nghia Le, Tam V. Nguyen, Zhongliang Nie, Minh-Triet Tran, and Akihiro Sugimoto. Anabanch network for camouflaged object segmentation. *Comput. Vis. Image Underst.*, 184:45–56, 2019.

Chuyi Li, Lulu Li, Hongliang Jiang, Kaiheng Weng, Yifei Geng, Liang Li, Zaidan Ke, Qingyuan Li, Meng Cheng, Weiqiang Nie, et al. Yolov6: A single-stage object detection framework for industrial applications. *arXiv preprint arXiv:2209.02976*, 2022a.

Gongyang Li, Zhi Liu, Minyu Chen, Zhen Bai, Weisi Lin, and Haibin Ling. Hierarchical alternate interaction network for RGB-D salient object detection. *IEEE Trans. Image Process.*, 30:3528–3542, 2021.

Guanbin Li and Yizhou Yu. Visual saliency based on multiscale deep features. In *IEEE Conference on Computer Vision and Pattern Recognition, CVPR 2015, Boston, MA, USA, June 7–12, 2015*, pages 5455–5463. IEEE Computer Society, 2015.

Lin Li, Bo Dong, Eric Rigall, Tao Zhou, Junyu Dong, and Geng Chen. Marine animal segmentation. *IEEE Trans. Circuits Syst. Video Technol.*, 32(4):2303–2314, 2022b.

Ming Li, Hanqi Zhang, Armin Gruen, and Deren Li and. A survey on underwater coral image segmentation based on deep learning. *Geo-spatial Information Science*, 0(0):1–25, 2024.

Yin Li, Xiaodi Hou, Christof Koch, James M. Rehg, and Alan L. Yuille. The secrets of salient object segmentation. In *2014 IEEE Conference on Computer Vision and Pattern Recognition, CVPR 2014, Columbus, OH, USA, June 23-28, 2014*, pages 280–287. IEEE Computer Society, 2014.

Ting-Yu Liao, Ching-Hui Yang, Yu-Wen Lo, Kuan-Ying Lai, Po-Huai Shen, and Youn-Long Lin. Hardnet-dfus: Enhancing backbone and decoder of hardnet-mseg for diabetic foot ulcer image segmentation. In *MICCAI 2022*, volume 13797, pages 21–30. Springer, 2022.

Jiawei Liu, Jing Zhang, and Nick Barnes. Modeling aleatoric uncertainty for camouflaged object detection. In *WACV 2022*, pages 2613–2622. IEEE, 2022.

Songtao Liu, Di Huang, and Yunhong Wang. Receptive field block net for accurate and fast object detection. In Vittorio Ferrari, Martial Hebert, Cristian Sminchisescu, and Yair Weiss, editors, *ECCV 2018*, volume 11215 of *Lecture Notes in Computer Science*, pages 404–419. Springer, 2018.

Ange Lou, Shuyue Guan, and Murray H. Loew. Caranet: Context axial reverse attention network for segmentation of small medical objects. *CoRR*, abs/2301.13366, 2023.

Yunqiu Lv, Jing Zhang, Yuchao Dai, Aixuan Li, Bowen Liu, Nick Barnes, and Deng-Ping Fan. Simultaneously localize, segment and rank the camouflaged objects. In *IEEE Conference on Computer Vision and Pattern Recognition, CVPR 2021, virtual, June 19-25, 2021*, pages 11591–11601. Computer Vision Foundation / IEEE, 2021a.

Yunqiu Lv, Jing Zhang, Yuchao Dai, Aixuan Li, Bowen Liu, Nick Barnes, and Deng-Ping Fan. Simultaneously localize, segment and rank the camouflaged objects. In *CVPR 2021*, pages 11591–11601. Computer Vision Foundation / IEEE, 2021b.

Kresimir Matkovic, László Neumann, Attila Neumann, Thomas Psik, and Werner Purgathofer. Global contrast factor - a new approach to image contrast. In *CAe 2005*, pages 159–167. Eurographics Association, 2005.

Haiyang Mei, Ge-Peng Ji, Ziqi Wei, Xin Yang, Xiaopeng Wei, and Deng-Ping Fan. Camouflaged object segmentation with distraction mining. In *CVPR 2021*, pages 8772–8781. Computer Vision Foundation / IEEE, 2021.

Zizheng Pan, Jianfei Cai, and Bohan Zhuang. Fast vision transformers with hilo attention. In *NeurIPS 2022*, 2022.

Youwei Pang, Xiaoqi Zhao, Tian-Zhu Xiang, Lihe Zhang, and Huchuan Lu. Zoom in and out: A mixed-scale triplet network for camouflaged object detection. In *CVPR 2022*, pages 2150–2160. IEEE, 2022.

Krushi Patel, Andrés M. Bur, and Guanghui Wang. Enhanced u-net: A feature enhancement network for polyp segmentation. In *CRV 2021*, pages 181–188. IEEE, 2021.

Yongri Piao, Jian Wang, Miao Zhang, and Huchuan Lu. Mfnet: Multi-filter directive network for weakly supervised salient object detection. In *ICCV 2021*, pages 4116–4125. IEEE, 2021.

Xuebin Qin, Zichen Zhang, Chenyang Huang, Masood Dehghan, Osmar R. Zaïane, and Martin Jägersand. U<sup>2</sup>-net: Going deeper with nested u-structure for salient object detection. *Pattern Recognit.*, 106:107404, 2020.

Zhongxi Qiu, Yan Hu, Heng Li, and Jiang Liu. Learnable ophthalmology SAM. *CoRR*, abs/2304.13425, 2023.

Sylvestre-Alvise Rebuffi, Hakan Bilen, and Andrea Vedaldi. Efficient parametrization of multi-domain deep neural networks. In *2018 IEEE CVPR 2018*, pages 8119–8127. Computer Vision Foundation / IEEE Computer Society, 2018.

Olaf Ronneberger, Philipp Fischer, and Thomas Brox. U-net: Convolutional networks for biomedical image segmentation. In *MICCAI 2015*, volume 9351, pages 234–241. Springer, 2015.

Juan Silva, Aymeric Histace, Olivier Romain, Xavier Dray, and Bertrand Granado. Toward embedded detection of polyps in WCE images for early diagnosis of colorectal cancer. *Int. J. Comput. Assist. Radiol. Surg.*, 9(2):283–293, 2014.

Przemysław Skurowski, Hassan Abdulameer, Jakub Błaszczyk, Tomasz Depta, Adam Kornacki, and Przemysław Koziel. Animal camouflage analysis: Chameleon database. *Unpublished manuscript*, 2(6):7, 2018.

Yujia Sun, Geng Chen, Tao Zhou, Yi Zhang, and Nian Liu. Context-aware cross-level fusion network for camouflaged object detection. In *IJCAI 2021*, pages 1025–1031. ijcai.org, 2021.

Nima Tajbakhsh, Suryakanth R. Gurudu, and Jianming Liang. Automated polyp detection in colonoscopy videos using shape and context information. *IEEE Trans. Medical Imaging*, 35(2):630–644, 2016.

Vincent Tonkes and Matthias Sabatelli. How well do vision transformers (vtvs) transfer to the non-natural image domain? an empirical study involving art classification. In *ECCV 2022*, volume 13801, pages 234–250. Springer, 2022.

David Vázquez, Jorge Bernal, Francisco Javier Sánchez, Gloria Fernández-Esparrach, Antonio M. López, Adriana Romero, Michal Drozdzał, and Aaron C. Courville. A benchmark for endoluminal scene segmentation of colonoscopy images. *CoRR*, abs/1612.00799, 2016.

Feng Wang, Xianan Sun, and Jinhua Li. Surgical smoke removal via residual swin transformer network. *Int. J. Comput. Assist. Radiol. Surg.*, 18(8):1417–1427, 2023a.

Lijun Wang, Huchuan Lu, Yifan Wang, Mengyang Feng, Dong Wang, Baocai Yin, and Xiang Ruan. Learning to detect salient objects with image-level supervision. In *2017 IEEE Conference on Computer Vision and Pattern Recognition, CVPR 2017, Honolulu, HI, USA, July 21-26, 2017*, pages 3796–3805. IEEE Computer Society, 2017.

Yi Wang, Ruili Wang, Xin Fan, Tianzhu Wang, and Xiangjian He. Pixels, regions, and objects: Multiple enhancement for salient object detection. In *IEEE/CVF Conference on Computer Vision and Pattern Recognition, CVPR 2023, Vancouver, BC, Canada, June 17-24, 2023*, pages 10031–10040. IEEE, 2023b.

Jun Wei, Yiwen Hu, Ruimao Zhang, Zhen Li, S. Kevin Zhou, and Shuguang Cui. Shallow attention network for polyp segmentation. In *MICCAI 2021*, volume 12901, pages 699–708. Springer, 2021.

Xiaobao Wei, Jiajun Cao, Yizhu Jin, Ming Lu, Guangyu Wang, and Shanghang Zhang. I-medSAM: Implicit medical image segmentation with segment anything. In *ECCV 2024*, volume 15068, pages 90–107. Springer, 2024.

Junde Wu, Rao Fu, Huihui Fang, Yuanpei Liu, Zhaowei Wang, Yanwu Xu, Yueming Jin, and Tal Arbel. Medical SAM adapter: Adapting segment anything model for medical image segmentation. *CoRR*, abs/2304.12620, 2023a.

Junde Wu, Rao Fu, Huihui Fang, Yuanpei Liu, Zhaowei Wang, Yanwu Xu, Yueming Jin, and Tal Arbel. Medical SAM adapter: Adapting segment anything model for medical image segmentation. *CoRR*, abs/2304.12620, 2023b.

Yu-Huan Wu, Yun Liu, Le Zhang, Ming-Ming Cheng, and Bo Ren. EDN: salient object detection via extremely-downsampled network. *IEEE Trans. Image Process.*, 31:3125–3136, 2022.

Zhe Wu, Li Su, and Qingming Huang. Stacked cross refinement network for edge-aware salient object detection. In *ICCV 2019*, pages 7263–7272. IEEE, 2019.

Xinyu Xiong, Zihuang Wu, Shuangyi Tan, Wenxue Li, Feilong Tang, Ying Chen, Siying Li, Jie Ma, and Guanbin Li. Sam2-unet: Segment anything 2 makes strong encoder for natural and medical image segmentation. *CoRR*, abs/2408.08870, 2024.

Qiong Yan, Li Xu, Jianping Shi, and Jiaya Jia. Hierarchical saliency detection. In *2013 IEEE Conference on Computer Vision and Pattern Recognition, Portland, OR, USA, June 23-28, 2013*, pages 1155–1162. IEEE Computer Society, 2013.

Tianyu Yan, Zifu Wan, Xinhao Deng, Pingping Zhang, Yang Liu, and Huchuan Lu. MAS-SAM: segment any marine animal with aggregated features. In *IJCAI 2024*, pages 6886–6894. ijcai.org, 2024.

Jianwei Yang, Chunyuan Li, Xiyang Dai, and Jianfeng Gao. Focal modulation networks. In *NeurIPS 2022*, 2022.

Zijin Yin, Kongming Liang, Zhanyu Ma, and Jun Guo. Duplex contextual relation network for polyp segmentation. In *ISBI 2022*, pages 1–5. IEEE, 2022.

Guhnoo Yun, Juhan Yoo, Kijung Kim, Jeongho Lee, and Dong Hwan Kim. Spanet: Frequency-balancing token mixer using spectral pooling aggregation modulation. In *ICCV 2023*, pages 6090–6101. IEEE, 2023.

Pingping Zhang, Tianyu Yan, Yang Liu, and Huchuan Lu. Fantastic animals and where to find them: Segment any marine animal with dual SAM. In *CVPR 2024*, pages 2578–2587. IEEE, 2024.

Ruifei Zhang, Peiwen Lai, Xiang Wan, De-Jun Fan, Feng Gao, Xiao-Jian Wu, and Guanbin Li. Lesion-aware dynamic kernel for polyp segmentation. In *MICCAI 2022*, volume 13433, pages 99–109. Springer, 2022.

Ruifei Zhang, Guanbin Li, Zhen Li, Shuguang Cui, Dahong Qian, and Yizhou Yu. Adaptive context selection for polyp segmentation. *CoRR*, abs/2301.04799, 2023.

Ting Zhao and Xiangqian Wu. Pyramid feature attention network for saliency detection. In *CVPR 2019*, pages 3085–3094. Computer Vision Foundation / IEEE, 2019.

Xiaoqi Zhao, Lihe Zhang, and Huchuan Lu. Automatic polyp segmentation via multi-scale subtraction network. In *MICCAI 2021*, volume 12901, pages 120–130. Springer, 2021.

Sixiao Zheng, Jiachen Lu, Hengshuang Zhao, Xiatian Zhu, Zekun Luo, Yabiao Wang, Yanwei Fu, Jianfeng Feng, Tao Xiang, Philip H. S. Torr, and Li Zhang. Rethinking semantic segmentation from a sequence-to-sequence perspective with transformers. In *CVPR 2021*, pages 6881–6890. Computer Vision Foundation / IEEE, 2021.

Tao Zhou, Yi Zhou, Chen Gong, Jian Yang, and Yu Zhang. Feature aggregation and propagation network for camouflaged object detection. *IEEE Trans. Image Process.*, 31:7036–7047, 2022.

Tao Zhou, Yizhe Zhang, Yi Zhou, Ye Wu, and Chen Gong. Can SAM segment polyps? *CoRR*, abs/2304.07583, 2023a.

Tao Zhou, Yi Zhou, Kelei He, Chen Gong, Jian Yang, Huazhu Fu, and Dinggang Shen. Cross-level feature aggregation network for polyp segmentation. *Pattern Recognit.*, 140:109555, 2023b.

Zongwei Zhou, Md Mahfuzur Rahman Siddiquee, Nima Tajbakhsh, and Jianming Liang. Unet++: Redesigning skip connections to exploit multiscale features in image segmentation. *IEEE Trans. Medical Imaging*, 39(6):1856–1867, 2020.

Mingchen Zhuge, Deng-Ping Fan, Nian Liu, Dingwen Zhang, Dong Xu, and Ling Shao. Salient object detection via integrity learning. *IEEE Trans. Pattern Anal. Mach. Intell.*, 45(3):3738–3752, 2023.

## A Technical Appendices and Supplementary Material

### A.1 DWTConv.

To fully utilize low-frequency features, we employ specific cascaded deep wavelet convolution operations. We use the Haar wavelet transform for simplicity and efficiency while utilizing four sets of filters for filtering in different frequency bands.

$$\begin{aligned} f_{LL} &= \frac{1}{2} \begin{bmatrix} 1 & 1 \\ 1 & 1 \end{bmatrix}, & f_{LH} &= \frac{1}{2} \begin{bmatrix} 1 & -1 \\ 1 & -1 \end{bmatrix}, \\ f_{HL} &= \frac{1}{2} \begin{bmatrix} 1 & 1 \\ -1 & -1 \end{bmatrix}, & f_{HH} &= \frac{1}{2} \begin{bmatrix} 1 & -1 \\ -1 & 1 \end{bmatrix}. \end{aligned} \quad (14)$$

Among them,  $f_{LL}$  is the low-pass filter, while the others are high-pass filters. Subsequently, a convolution with a kernel size of 1 is used for deep aggregation operations. For different input channels, the output is

$$\begin{aligned} [X_{LL}, X_{LH}, X_{HL}, X_{HH}] &= \\ \text{Conv}_{(1 \times 1)}([f_{LL}, f_{LH}, f_{HL}, f_{HH}], X) &. \end{aligned} \quad (15)$$

To align the output with the input dimensions, we use inverse wavelet transform to aggregate the features after wavelet decomposition, thus constructing the output

$$Y = \text{IWT}(\text{Conv}_{(1 \times 1)}(W, \text{WT}(X))). \quad (16)$$

The above formula represents only a single-level wavelet decomposition and aggregation operation.

In the WASF, we employ cascaded wavelet decomposition to sequentially decompose the low-frequency signal  $X_{LL}^{(i)}$  (where  $i$  indicates the level). This enhances the low-frequency features while simultaneously reducing the spatial resolution to some extent. The process of cascaded wavelet decomposition and aggregation is as follows:

$$X_{LL}^{(i)}, X_H^{(i)} = \text{WT}(X_{LL}^{(i-1)}), \quad (17)$$

$$Y_{LL}^{(i)}, Y_H^{(i)} = \text{Conv}_{(1 \times 1)}(W^{(i)}, (X_{LL}^{(i)}, X_H^{(i)})), \quad (18)$$

$$z^{(i)} = \text{IWT}(Y_{LL}^{(i)} + z^{(i+1)}, Y_H^{(i)}). \quad (19)$$

Note that the above inverse wavelet transform formula simplifies using the theorem that states the inverse wavelet transform is a linear operation:

$$\text{IWT}(X + Y) = \text{IWT}(X) + \text{IWT}(Y). \quad (20)$$

In the DWTConv module, we employ deep convolution operations with a receptive field size of  $n \times n$  to simulate the different receptive field features captured by the human eye. To reduce the parameter count of the model without compromising its performance, we use deep convolution operations with kernel sizes of  $1 \times n$  and  $n \times 1$ .

### A.2 Experiments

#### A.2.1 Datasets and Evaluation Metrics.

Following the convention Yang et al. [2022], Yun et al. [2023], we experimentally validated the effectiveness of FE-UNet on two tasks: marine animal segmentation and polyp segmentation.

The content in Table 4 shows the dataset configuration used in our experiments.

Marine Animal Segmentation Deep-sea exploration robots are tasked with separating marine animals from their deep-sea environments to analyze biodiversity and protect endangered species. However, during operations, high-frequency attenuation caused by the combined effects of underwater non-uniform illumination and seawater scattering/absorption/refraction poses challenges. To evaluate our model's performance in low-frequency information-rich deep-sea environments, we employed four public benchmark datasets: MAS3K, RMAS, UFO120, and RUWI datasets.

Table 4: Task Set

Tasks	Dataset	Train Set	Test Set
Marine Animal Segmentation	MAS3K	1769	1141
	RMAS	2514	500
Polyp Segmentation	Kvasir-SEG	900	100
	CVC-ClinicDB	550	62
	CVC-ColonDB	-	380
	CVC-300	-	60
	ETIS	-	196
Camouflaged Object Detection	CAMO	1000	250
	COD10K	3040	2026
	CHAMELEON	-	76
	NC4K	-	4121
Salient Object Detection	DUTS	10533	5019
	DUT-OMRON	-	5168
	HKU-IS	-	4447
	PASCAL-S	-	850
	ECSSD	-	1000

- MAS3K: This dataset contains 3,103 high-quality annotated images. We followed the default split, using 1,769 images for training and 1,141 images for testing, while excluding the remaining 193 images that contained only backgrounds.
- RMAS: This dataset includes 3,014 marine images. We used 2,514 images to train the model and 500 images to test the model’s performance.
- UFO120: This dataset consists of 1,620 underwater images featuring various scenes. We followed the default split, using 1,500 images for training and 120 images to evaluate the model’s performance.
- RUWI: This dataset comprises real underwater images captured under complex lighting conditions, containing 700 images. Unlike the original paper, we used 525 images for model training and 175 images for testing.

**Polyp Segmentation** Polyp segmentation aims to identify and outline polyps within endoscopic images, supporting the early detection and management of colorectal cancer. Challenges emerge from the diverse appearances of polyps, the subtle contrast with surrounding mucosa, and imaging issues like motion blur and uneven lighting. To assess our model’s effectiveness in these intricate endoscopic settings, we utilized five public benchmark datasets: Kvasir-SEG, CVC-ClinicDB, CVC-ColonDB, CVC-300, and ETIS datasets.

- Kvasir-SEG: This datasets contains 1,000 images, with resolutions ranging from 720x576 to 1,920x1,072 pixels, covering various anatomical landmarks and pathological findings such as polyps, esophagitis, and ulcerative colitis. We used 900 images for model training and 100 images for testing ,as done in the SAM2-Unet paper.
- CVC-ClinicDB: This dataset includes 612 images with a resolution of 384x288 pixels, extracted from 31 colonoscopy sequences. It is widely used for medical image segmentation, particularly for polyp detection in colonoscopy videos, providing binary masks for precise polyp localization. We used 550 images for model training and 62 images for testing ,as done in the SAM2-Unet paper.
- CVC-ColonDB: This dataset his dataset consists of annotated frames extracted from 15 short colonoscopy sequences. We used this dataset for testing.
- CVC-300: This dataset contains 60 images used for testing polyp segmentation models. We also used this dataset for testing.
- ETIS: This dataset includes 196 images focused on polyp segmentation in colonoscopy videos. It is a challenging dataset due to the variability in polyp appearance and imaging conditions. We used this dataset to test the generalization of our model.

Camouflaged Object Detection Camouflaged object detection is tasked with identifying and separating camouflaged objects from their natural environments to analyze biodiversity and support conservation efforts. However, during operations, the intricate blending of objects with their backgrounds due to non-uniform illumination and varying environmental factors like texture and color mimicry presents significant challenges. To evaluate our model’s performance in complex, low-frequency information-rich environments, we employed four benchmark datasets: CAMO, COD10K, CHAMELEON, and NC4K datasets.

- CAMO: This datasets contains 1,250 images for camouflaged object segmentation, focusing on natural and artificial camouflage. We followed the default split, using 1,000 images for training and 250 images for testing.
- COD10K: This dataset includes 10,000 images diverse camouflaged objects. We used 3,040 images for model training and 2,026 images for testing as done in the SAM2-Unet paper.
- CHAMELEON: This dataset consists of 76 high-quality annotated images. We used this dataset for preliminary detection testing
- NC4K: This dataset with 4,121 images to evaluate model generalization in camouflaged object detection, We used this dataset for testing.

Salient Object Detection Salient Object Detection (SOD) is a vision task focused on detecting and segmenting visually prominent objects that attract human attention, leveraging advanced feature extraction and multi-scale contextual analysis to generate precise binary masks in challenging, cluttered backgrounds. The primary challenge in SOD is accurately distinguishing visually prominent objects from highly cluttered or low-contrast backgrounds with robust feature discrimination and precise boundary delineation. To evaluate our model’s performance in complex, low-frequency information-rich environments, we employed five public benchmark datasets: DUTS, DUT-OMRON, HKU-IS, PASCAL-S and ECSSD.

- DUTS: This datasets is the largest saliency detection benchmark with 10,553 training and 5,019 test images, featuring challenging scenarios and pixel-level ground truths annotated by 50 subjects. We followed the default split, using 10,553 images for training and 5,019 images to test the model’s performance.
- DUT-OMRON: This dataset contains 5,168 high-quality images with one or more salient objects in complex backgrounds, annotated with pixel-wise, bounding box, and eye-fixation ground truths. We used this dataset for testing.
- HKU-IS: This dataset contains 4,447 images, emphasizing low-contrast scenes or multiple salient objects with high-quality pixel-level annotations. We used this dataset for testing.
- PASCAL-S: This dataset contains 850 images from PASCAL VOC 2010, featuring multiple salient objects in diverse scenes with detailed saliency annotations. We used this dataset for testing.
- ECSSD: This dataset includes 1,000 intricate images with complex textures and structures. We used this dataset for testing.

### A.2.2 Implementation Details

For the Wavelet-Adaptive Spectral Fusion (WASF), we set the specificity of the cascaded depth wavelet convolution kernel to  $1 \times 1$  with a stride of 1. Additionally, we employ three parallel SPF modules, configuring  $\lambda$  to 0.7 and 0.9, respectively.

The model is implemented based on the PyTorch framework, which is widely used in the field of deep learning due to its strong flexibility and ease of use.

The model is trained using the AdamW optimizer, an improved version of the Adam optimizer that includes a weight decay mechanism to better prevent overfitting. The initial learning rate for AdamW is set to 0.001.

We use a batch size of 8, which determines the number of samples used for each training iteration when updating the model parameters, influencing the model’s convergence speed and training efficiency.

The training is set for 30 epochs to better adapt to the marine animal segmentation and polyp segmentation tasks.

All input images are resized to 350×350, which helps reduce computational overhead while ensuring that image information is preserved.

The model employs a cosine decay learning rate strategy to gradually decrease the learning rate during the later stages of training, ensuring more stable training and avoiding oscillations or overfitting.

All experiments were conducted on a system equipped with an Intel(R) Xeon(R) Platinum 8462Y+ CPU, 8 NVIDIA A800-SXM4-80GB GPUs, and 1TB of RAM.

Table 5: Camouflaged object detection performance on CHAMELEON Skurowski et al. [2018] and CAMO Le et al. [2019] datasets.

Method	CHAMELEON				CAMO			
	$S_\alpha$	$F_\beta$	$E_\phi$	MAE	$S_\alpha$	$F_\beta$	$E_\phi$	MAE
SINetFan et al. [2020a]	0.872	0.823	0.936	0.034	0.745	0.712	0.804	0.092
PFNetMei et al. [2021]	0.882	0.820	0.931	0.033	0.782	0.751	0.841	0.085
ZoomNetPang et al. [2022]	0.902	0.858	0.943	0.024	0.820	0.792	0.877	0.066
FDERHe et al. [2023b]	0.903	0.856	0.947	0.026	0.836	0.807	0.897	0.066
SAM2-UNetXiong et al. [2024]	0.914	0.863	<b>0.961</b>	<u>0.022</u>	0.884	<b>0.861</b>	<b>0.932</b>	0.042
FE-UNet(Ours)	<b>0.921</b>	<b>0.880</b>	<u>0.958</u>	<b>0.020</b>	<b>0.891</b>	0.855	<u>0.931</u>	<b>0.038</b>

Table 6: Camouflaged object detection performance on COD10K Fan et al. [2020a] and NC4K Lv et al. [2021a] datasets.

Method	COD10K				NC4K			
	$S_\alpha$	$F_\beta$	$E_\phi$	MAE	$S_\alpha$	$F_\beta$	$E_\phi$	MAE
SINetFan et al. [2020a]	0.776	0.667	0.864	0.043	0.808	0.768	0.871	0.058
PFNetMei et al. [2021]	0.800	0.676	0.877	0.040	0.829	0.779	0.887	0.053
ZoomNetPang et al. [2022]	0.838	0.740	0.888	0.029	0.853	0.814	0.896	0.043
FDERHe et al. [2023b]	<u>0.844</u>	0.748	0.911	0.029	0.862	0.824	0.913	0.042
SAM2-UNetXiong et al. [2024]	<b>0.880</b>	<u>0.789</u>	<b>0.936</b>	<u>0.021</u>	<u>0.901</u>	<u>0.863</u>	<b>0.941</b>	<u>0.029</u>
FE-UNet(Ours)	<b>0.880</b>	<b>0.804</b>	0.932	<b>0.020</b>	<b>0.902</b>	<b>0.866</b>	0.935	<b>0.028</b>

Table 7: Salient object detection performance on DUTS-TE Wang et al. [2017], DUT-OMRON Deng et al. [2020], and HKU-IS Li and Yu [2015] datasets.

Method	DUTS-TE			DUT-OMRON			HKU-IS		
	$S_\alpha$	$E_\phi$	MAE	$S_\alpha$	$E_\phi$	MAE	$S_\alpha$	$E_\phi$	MAE
U2NetQin et al. [2020]	0.874	0.884	0.044	0.847	0.872	0.054	0.916	0.948	0.031
ICONZhuge et al. [2023]	0.889	0.914	0.037	0.845	0.879	0.057	0.920	0.959	0.029
EDNWu et al. [2022]	0.892	0.925	0.035	0.850	0.877	0.049	0.924	0.955	0.026
MENetWang et al. [2023b]	<u>0.905</u>	0.937	0.028	0.850	0.891	0.045	0.927	0.966	0.023
SAM2-UNetXiong et al. [2024]	<b>0.934</b>	<b>0.959</b>	<u>0.020</u>	0.884	<u>0.912</u>	<u>0.039</u>	<u>0.941</u>	<b>0.971</b>	<u>0.019</u>
FE-UNet(Ours)	<b>0.934</b>	<u>0.952</u>	<b>0.019</b>	<b>0.892</b>	<b>0.918</b>	<b>0.034</b>	<b>0.946</b>	<u>0.970</u>	<b>0.018</b>

Similar to SAM2-UNetXiong et al. [2024], we also conducted experiments on both salient object detection and camouflaged object detection tasks. The experimental results demonstrate that our model exhibits superior performance compared to SAM2-UNet on datasets of these tasks. Specifically, our model achieves better results than SAM2-UNet in terms of the Mean Absolute Error (MAE) and Structural Similarity Index ( $S_\alpha$ ) across all task metrics. This demonstrates that the proposed model and its modules are effective across multiple tasks.

Table 8: Salient object detection performance on PASCAL-S Li et al. [2014] and ECSSD Yan et al. [2013] datasets.

Method	PASCAL-S			ECSSD		
	$S_\alpha$	$E_\phi$	MAE	$S_\alpha$	$E_\phi$	MAE
U2NetQin et al. [2020]	0.844	0.850	0.074	0.928	0.925	0.033
ICONZhuge et al. [2023]	0.861	0.893	0.064	0.929	0.954	0.032
EDNWu et al. [2022]	0.865	0.902	0.062	0.927	0.951	0.032
MENetWang et al. [2023b]	0.872	0.913	0.054	0.928	0.954	0.031
SAM2-UNetXiong et al. [2024]	0.894	0.931	<b>0.043</b>	0.950	<b>0.970</b>	0.020
FE-UNet(Ours)	<b>0.895</b>	<b>0.933</b>	0.044	<b>0.954</b>	0.956	<b>0.019</b>